Hybrid Kinematic-Dynamic Sideslip and Friction Estimation

Stefano Carnier
PhD Student
DEIB
Politecnico di Milano
Piazza L. da Vinci 32, 20133 Milano, Italy.
Email: stefano.carnier@polimi.it

Matteo Corno
Associate Professor
DEIB
Politecnico di Milano
Piazza L. da Vinci 32, 20133 Milano, Italy.
Email: matteo.corno@polimi.it

Sergio M. Savaresi
Professor
DEIB
Politecnico di Milano
Piazza L. da Vinci 32, 20133 Milano, Italy.
Email: sergio.savaresi@polimi.it

Vehicle sideslip and tyre/road friction are crucial variables for advanced vehicle stability control systems. Estimation is required since direct measurement through sensors is costly and unreliable. In this paper, we develop and validate a sideslip estimator robust to unknown road grip conditions. Particularly, the paper addresses the problem of rapid tyre/road friction adaptation when sudden road condition variations happen. The algorithm is based on a hybrid kinematic-dynamic closed loop observer augmented with a tyre/road friction classifier that reinitializes the states of the estimator when a change of friction is detected. Extensive experiments on a 4 wheel drive electric vehicle carried out on different roads quantitatively validate the approach. The architecture guarantees accurate estimation on dry and wet asphalt and snow terrain with a maximum sideslip estimation error lower than 1.5 *deg. The classifier correctly recognizes* 87% *of the friction changes; wrongly classifies 2% of the friction changes while it is unable to detect the change in 11% of the cases. The missed detections are due to the fact that the algorithm requires a certain level of vehicle excitation to detect a change of friction. The average classification time is* 1.6 *s. The tests also indicate the advantages of the friction classifiers on the sideslip estimation error.*

1 INTRODUCTION

Improving vehicle stability performance is one of the focuses of automotive research. Special attention is paid to emergency maneuvers through the adoption of advanced technologies such as active steering, torque vectoring or active differentials [1, 2]. Vehicle stabilization is becoming more and more important for autonomous vehicles which, in emergency situations, have to perform maneuvers close to their handling limits to avoid collisions. In such scenarios, actions needed to stabilize the vehicle dynamic may not coincide with those necessary for obstacle avoidance making the control system design even more challenging [3–5].

All stability control systems rely on real-time vehicle state information [6]. Needless to say, the sideslip angle (defined as the angle between the vehicle longitudinal axis and the direction of the velocity vector) is of utmost importance in this context [7]. Unfortunately, direct sensing of the sideslip angle is not, so far, industrially viable due to high cost and lack of reliability. Estimation is then required to overcome this issue.

Sideslip estimation has received a considerable amount of attention over the years, with many interesting and effective contributions which can be classified in two main categories [8]: black-box approaches and model-based approaches.

Black-box estimators are based on non-linear functions (e.g. neural network) optimized to fit the experimental data, notable examples can be found in [9–12]. They do not require any vehicle model, but the estimation accuracy strongly depends on how comprehensive the training dataset is. Moreover, the need of retraining the observer in case of changes in vehicle or driving conditions represents a significant drawback of black-box strategies.

Model-based approaches rely on vehicle kinematic and dynamic models to develop estimators in the classical feedback framework.

Kinematic estimators [13, 14] are based on a description of the vehicle motion relating kinematic quantities and do not depend on specific vehicle or tire parameters facilitating their implementation on different vehicles without the need of relevant retuning procedures. However, estimators designed uniquely on kinematic models tend to drift when the vehicle lateral dynamic is not properly excited [15]. A possible solution is to include Global Navigation Satellite Systems measurement [16] which however is not always reliable.

Dynamic estimators [**?**, 17–21] overcome the estimation drift problem relying on more complex dynamic models. The estimation accuracy of such approaches is strictly related to the model complexity and to the prior knowledge of the constituting vehicle parameters. The road-tire forces characteristic is the most critical aspect. It is achieved through non-linear tire models [22] whose parameters significantly vary depending on tire and road friction conditions. To guarantee robustness, dynamic observers often require an additional real-time tyre/road friction estimate [23].

Hybrid approaches [24, 25] aim at taking the most of both kind of models. The information coming from the kinematic model is combined with the output of a simple lateral tire-road friction dynamic model. In this way, hybrid model-based methods are less sensitive to tuning than dynamic based approaches. Although hybrid models, thanks to their kinematic component, are inherently more robust to variation in the friction coefficient, their accuracy can be affected by changes of friction. The introduction of friction estimation modules [26–32] improves the overall robustness, beside offering an explicit estimation of a parameter useful to vehicle dynamics control. The approach presented in [26,33] is among the most interesting and successful ones. The feedback observer estimates sideslip and friction together relying on a frequency decoupling idea. Slow variations in vehicle lateral dynamics feedback innovation term are assumed to reflect changes of road friction while fast ones are due to vehicle lateral drifts. Hence, the estimated tyre/road friction requires a significant time interval to adapt to road condition changes. This becomes a relevant limitation when abrupt variations of road surface conditions occur. The friction estimate slowly settles to the new value and the sideslip estimation accuracy decreases all along this phase.

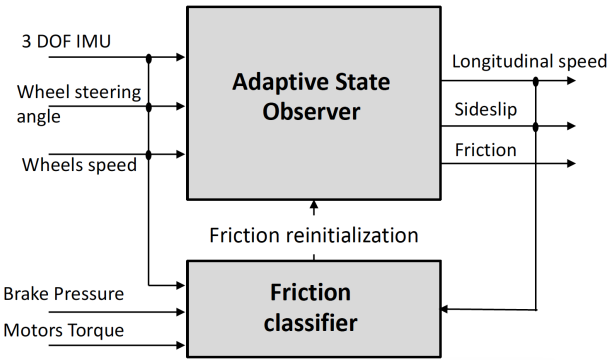

Fig. 1: Full observer structure.

This paper extends [26, 33] addressing the problem of reducing the friction adaptation time to guarantee robustness also to sudden changes of the road conditions. Namely, an additional slip based friction classifier is developed and combined to the hybrid adaptive state observer, as summarized in the full architecture scheme in Figure 1. Slip-based classifiers provide a rapid road friction estimation [34–36] monitoring the correlation between tire slips and friction. However, a highly-parametrized structure and extensive training on data collected on various road conditions is necessary to achieve accurate estimation [37]. In this solution, the classifier aims only at promptly detecting changes in friction. Based on that, the adaptive observer friction state variable is instantaneously reinitialized to a value closer to the actual one. Then, the adaptive state observer converges to the real value. Hence, the goal of a rapid and accurate friction and sideslip estimation is achieved adding a classifier with a relatively simple architecture.

The main contribution of our work concerns the development, improvement and thorough experimental validation of the hybrid adaptive state observer and the introduction of the friction classifier. To summarize, we introduce

1. A scheduling logic of the observer feedback gains. Thanks to the scheduling logic, the observer makes the most of the hybrid structure. The estimate privileges either the kinematic or dynamic models contributions depending on the vehicle dynamics condition.

2. An improved road friction adaptation of the road-tire model. The road-tire model dependency on the friction is developed to achieve more accurate characteristics during the adaptation phase between high and low grip conditions.
3. An additional new friction classifier. The development and introduction of a friction classifier results in significant reduction of the adaptation time to sudden changes of road conditions. The refined friction estimation improves and makes the sideslip estimation more robust.

The paper is organized as follows. Section 2 and Section 3 deal with the two components of the estimator. The adaptive sideslip state observer is presented in Section 2 while Section 3 reports the friction classifier design. Section 4 presents the experimental campaign results.

2 ADAPTIVE STATE OBSERVER

Figure 1 shows that the architecture has two main modules: the adaptive state observer and the friction classifier.
The adaptive state observer inputs comes from car stock sensors: longitudinal and lateral barycentric accelerations A_x, A_y and yaw rate ω_z from a 3 degrees of freedom inertial measurements unit (IMU), steering angle δ_{st}, wheel speed V_{w_i} from encoders. The estimated outputs are the longitudinal speed V_x, the sideslip angle β and the friction coefficient μ. Figure 2 visualizes all the involved variables and the chosen sign conventions.

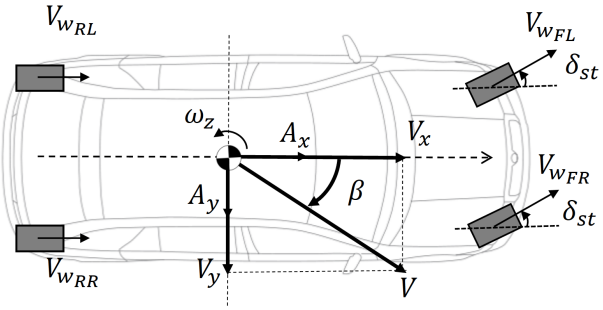

Fig. 2: Vehicle reference system: input and output variables.

Figure 3 shows the adaptive state observer general structure. Raw measures are pre-processed through standard filtering techniques and become inputs of the estimator which exploits both a kinematic and dynamic vehicle

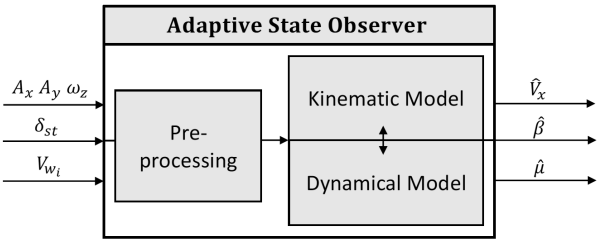

Fig. 3: Adaptive observer structure.

model. The baseline kinematic model:

$$\begin{cases} \dot{V}_x = -\omega_z \cdot V_y + A_x \\ \dot{V}_y = \omega_z \cdot V_x + A_y \end{cases} \tag{1}$$

assumes the vehicle to be a mass lumped in the Center of Gravity (CoG) moving in the 2D plane and describes the longitudinal and lateral speed dynamics V_x, V_y in the vehicle reference frame. The sideslip angle is defined as $\beta = \arctan\left(\frac{V_y}{V_x}\right)$ and can be directly obtained from a state observer based on a second order kinematic model.

However, it is well known that estimators developed based only on (1) tend to drift when driving straight or during steady state cornering [14, 15]. The following feedback state observer, by incorporating a dynamic model, alleviates this issue:

$$\begin{aligned} \begin{bmatrix} \dot{\hat{V}}_x \\ \dot{\hat{V}}_y \end{bmatrix} &= \begin{bmatrix} 0 & -\omega_z \\ \omega_z & 0 \end{bmatrix} \begin{bmatrix} \hat{V}_x \\ \hat{V}_y \end{bmatrix} + \begin{bmatrix} A_x \\ A_y \end{bmatrix} + \\ &+ \begin{bmatrix} K_x & 0 \\ 0 & K_y \end{bmatrix} \begin{bmatrix} \tilde{V}_x - \hat{V}_x \\ A_y - \hat{A}_y \end{bmatrix} \\ \dot{\hat{\mu}} &= K_\mu \cdot (A_y - \hat{A}_y) \\ \hat{\beta} &= \arctan \frac{\hat{V}_y}{\hat{V}_x}, \end{aligned} \tag{2}$$

and is the starting point of this work contribution.

The observer has three main components: the longitudinal and lateral speed $\hat{V}_x, \hat{V}_y$ and the friction $\hat{\mu}$ estimation. The estimation of V_x and V_y, in the first two equations, stem from augmenting the kinematic model with two output equations: $\tilde{V}_x$, $\hat{A}_y$. As in all closed-loop estimators, the apriori estimations are corrected by comparing the measured outputs with the predicted ones. Similarly, the friction estimation is corrected by comparing the predicted lateral acceleration against the measured

one. The tuning and scheduling of K_x, K_y, K_μ, the gain that determine how much one should *trust* the kinematic model against the predicted lateral acceleration, will allow for an accurate estimation of both vehicle states and road conditions. A detailed presentation of $\hat{V}_x, \hat{V}_y, \hat{\mu}$ estimation components, describing their feedback terms, follows.

2.1 Longitudinal Speed Estimation

$\tilde{V}_x$ and K_x are the two components of the longitudinal estimation feedback term. Ideally, one would want to

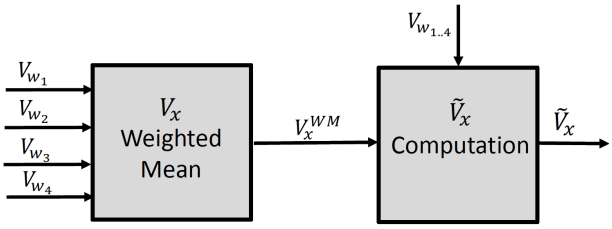

Fig. 4: V_x estimation from wheels speed: algorithm structure.

compare the estimated longitudinal speed against a measured longitudinal velocity. Unfortunately, such direct measurement is not available. An alternate measurement can be constructed using the 4 wheels velocities. Due to wheel slip occurring in case of particularly aggressive braking or traction maneuvers, wheel velocities measures may, in some cases, considerably differ from the vehicle speed. Therefore, $\tilde{V}_x$ is the result of a process that selects and properly merges the velocity measures coming from the non-slipping wheels to compute an initial approximation of the vehicle longitudinal speed. The algorithm consists of two phases as in Figure 4. The first module computes a weighted mean of the four wheel velocities:

$$V_x^{WM} = \frac{\sum_{i=1}^{4} k_{w_i} V_{w_i}}{\sum_{i=1}^{4} k_{w_i}}. \tag{3}$$

The mean attributes low weighting coefficients k_{w_i} to the wheels more likely to be slipping. One of the factors that impact wheel slip is load distribution: the lower the load, the more easily the wheel will slip. First the algorithm computes the direction of load transfer by considering the vehicle acceleration. Subsequently, all whees that are within an angular deviation of $[\gamma_-, \gamma_+]$ of the load transfer vector are given $k_{w_i} = 1$; all others, $k_{w_i} = 0$. Figure 5 exemplifies a braking maneuver, the load moves to the front, and, the front wheels fall into the confidence range ($k_{w_{FR,FL}} = 1$) while the rear ones do not ($k_{w_{RL,RR}} = 0$). The second module further elaborates the wheels speed

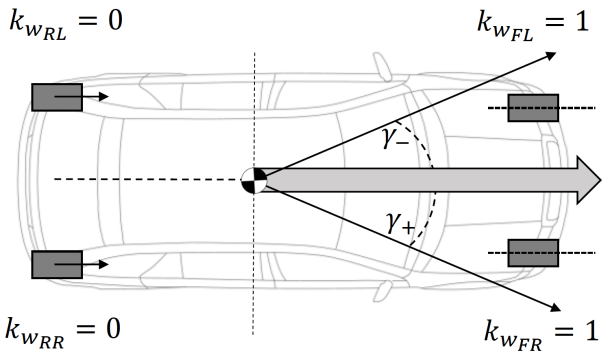

Fig. 5: V_x^{WM} wheel speed weighted mean: load based weighting coefficient k_{w_i} during braking maneuver on straight.

V_{w_i} and the weighted mean V_x^{WM} to provide the final outcome $\tilde{V}_x$. The procedure consists of two steps:

1. **Step 1:** the algorithm identifies and discards outliers among input quantities. It sorts the five signals V_{w_i}, V_x^{WM} in ascending order, takes the first and third quantiles $(Q1, Q3)$ and calculates the interquantile range $IQR = Q3 - Q1$. As in Figure 6, velocities outside the range $[Q1 - 1.5IQR, Q3 + 1.5IQR]$ are considered outliers and discarded. The scale of 1.5 is commonly used starting point for outlier detections and works well also in this application.

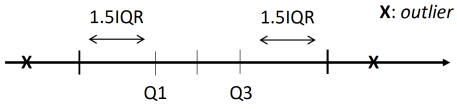

Fig. 6: $\tilde{V}_x$ outliers identification.

2. **Step 2:** $\tilde{V}_x$ is the result of a min-max logic similar to the [38] one and is here summarized to the readers' benefit:

$$\tilde{V}_x = \begin{cases} V_{min}, & A_x \geq 0 \\ V_{max}, & A_x < 0. \end{cases} \tag{4}$$

When the car is accelerating ($A_x > 0$) the wheels are likely to slip positively (i.e. wheels speed greater than vehicle one) and the minimum velocity (V_{min}) is more reliable. On the other hand, when the car is braking ($A_x < 0$), wheels longitudinal slip is negative (i.e. wheel speed lower than vehicle one) and the maximum speed (V_{max}) is closer to the actual vehicle speed V_x.

The second longitudinal feedback component is the feedback gain K_x. It weighs the contribution of the kinematic model compared to the innovation terms. A higher K_x privileges the information of the feedback signals $\tilde{V}_x$ while lower K_x forces the estimate to be closer to the integral of the kinematic model states. $\tilde{V}_x$ is computed using mainly the wheel velocities, when all four wheels are subject to considerable slip, its accuracy decreases. Hence, a scheduling logic is designed to have the most proper feedback gain values depending on the conditions. K_x takes a higher value ($K_{x_{max}}$) when $\tilde{V}_x$ is more reliable and a lower one ($K_{x_{min}}$) in opposite circumstances. The reliability of $\tilde{V}_x$ is estimated monitoring the difference between longitudinal acceleration from the IMU and the derivative of the wheel speed:

$$\Delta_{A_x} = \sum_{i=1}^{4} \left| \frac{d}{dt} V_i - A_x \right|. \tag{5}$$

If Δ_{A_x} is greater than a defined threshold ($\bar{\Delta}_{A_x}$) the wheels are likely to be slipping and this a lower feedback gain is employed:

$$K_x = \begin{cases} K_{x_{min}}, & \Delta_{A_x} \geq \bar{\Delta}_{A_x} \\ K_{x_{max}}, & \Delta_{A_x} < \bar{\Delta}_{A_x}. \end{cases} \tag{6}$$

2.2 Lateral Speed Estimation

The lateral speed feedback term consists of the difference between the measured lateral acceleration A_y and the predicted, based on the current state estimates, lateral acceleration $\hat{A}_y(\hat{V}_x, \hat{V}_y, \hat{\mu})$ multiplied by the feedback gain K_y.

$\hat{A}_y$ comes from a dynamic model where the wheels at each axle are lumped together as in Figure 7. Under the assumption of steady state turns (i.e. $\dot{\omega}_z = 0$) and neglecting vertical dynamics and longitudinal-lateral forces coupling, the lateral forces balance at the vehicle center of gravity yields:

$$\hat{A}_y = \frac{F_{y_F} \cos \delta_f + F_{y_R}}{m} \tag{7}$$

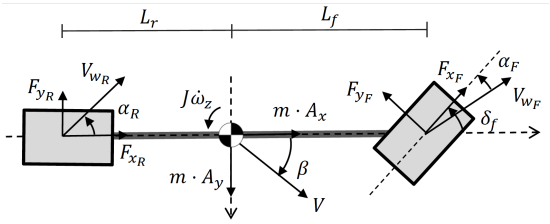

Fig. 7: Dynamic bicycle model.

where m is the vehicle mass, δ_f is the wheel steering angle and F_{y_F}, F_{y_R} are the road-tires lateral forces. The lateral forces model relies on the estimated $\hat{V}_x$ and $\hat{V}_y$ so that it imposes the feedback on the observer lateral dynamic equations. Moreover, it is designed to be dependent on the online estimated friction $\hat{\mu}$. F_{y_F}, F_{y_R} are functions of the wheels slip angles $\alpha_{F,R}$ (i.e. the angles between the wheel speed and its longitudinal axis):

$$F_{y_{F,R}} = \frac{C_{r_{F,R}}(\hat{\mu})}{k_{F,R}(\hat{\mu})} \cdot \tanh(k_{F,R}(\hat{\mu}) \cdot \alpha_{F,R}) \tag{8}$$

where $\alpha_{F,R}$ depends on $\hat{V}_x, \hat{\beta}$ through:

$$\begin{aligned} \alpha_F &= \delta_f - \hat{\beta} - L_f \frac{\omega_z}{\frac{\hat{V}_x}{cos\hat{\beta}}} \\ \alpha_R &= -\hat{\beta} - L_r \frac{\omega_z}{\frac{\hat{V}_x}{cos\hat{\beta}}} \end{aligned} \tag{9}$$

with L_f, L_r being the distances from the axle CoG. Note that two friction dependent parameters ($C_r(\hat{\mu}), k(\hat{\mu})$) define the $F_{y_{F,R}}$ characteristics. This strategy improves the one in [26] where $\hat{\mu}$ linearly scales a nominal characteristic of a dry road surface.

The proposed method consists in identifying the road-tire characteristics of two reference road surfaces with a high (μ_{high}) and a low (μ_{low}) friction from experimental data and to scale $C_r(\hat{\mu}), k(\hat{\mu})$ accordingly. The tire model coefficients will correspond to the ones identified on high grip surface when the estimated friction $\hat{\mu}$ is equal to μ_{high} and to the low friction ones if $\hat{\mu} = \mu_{low}$. The algorithm gets $C_r(\hat{\mu}), k(\hat{\mu})$ through linear interpolation if $\mu_{low} < \hat{\mu} < \mu_{high}$, and it extrapolates them if $\hat{\mu} > \mu_{high}$ or $\hat{\mu} < \mu_{low}$:

$$\begin{aligned} C_{r_{F,R}} &= a_{C_{F,R}} \cdot \hat{\mu} + b_{C_{F,R}} \\ k_{F,R} &= a_{k_{F,R}} \cdot \hat{\mu} + b_{k_{F,R}}. \end{aligned} \tag{10}$$

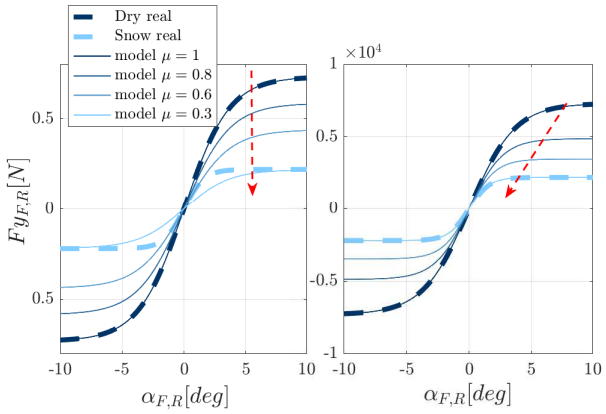

Fig. 8: State of the art: only $C_{f,r}$ is friction dependent (left). New model (8): both $C_{f,r}$ and $k_{f,r}$ are friction dependent (right)

The parameters $a_{C_{F,R}}, b_{C_{F,R}}, a_{k_{F,R}}, b_{k_{F,R}}$ define the linear $C_r(\hat{\mu}), k(\hat{\mu})$ dependency. Figure 8 compares the friction sensitivity analysis of two road-tire forces models. Figure 8, on the left, shows the state of the art approach where $\hat{\mu}$ linearly scales the $F_{y_{F,R}}$ characteristic while the right plot presents the proposed approach with $\hat{\mu}$ dependent $C_r(\hat{\mu}), k(\hat{\mu})$. The dashed dark and light blue lines are the reference characteristics identified on dry and snow surfaces while the continuous lines are the model output for different $\hat{\mu}$ values. One can see that:

1. When $\hat{\mu} = 1$, both models correspond to the reference dry road characteristic (dashed dark blue).
2. When $\hat{\mu} = 0.3$, the proposed model overlaps the snow reference (dashed light blue) while the output of the state of the art is different. The snow characteristic reaches its maximum for lower value of wheel slip angle ($\alpha \approxeq 1$ deg) with respect to the dry one ($\alpha_{F,R} \approxeq 6$ deg). The red arrow in Figure **??** shows that the state of the art method keeps such $\alpha_{F,R}$ value constant for every $\hat{\mu}$. In Figure **??**, on the contrary, variable $C_r(\hat{\mu}), k(\hat{\mu})$ adapts the maximum $F_{y_{F,R}}$ position (red arrow). This avoids modeling inaccuracies especially in case of surfaces with extremely low grip.

The feedback gain K_y is the product of three quantities:

$$K_y = \xi(\hat{V}_x, \hat{V}_y) \cdot \Delta(\hat{V}_x, \hat{V}_y) \cdot k_y. \tag{11}$$

$\xi(\hat{V}_x, \hat{V}_y)$ and $\Delta(\hat{V}_x, \hat{V}_y)$ are defined as in [26]. $\xi(\hat{V}_x, \hat{V}_y)$ is an approximation of the slope between $(\hat{V}_y, \hat{A}^*_y(\hat{V}_x, \hat{V}_y))$ and $(\hat{V}_y, \hat{A}^*_y(\hat{V}_x, V_y))$ where $\hat{A}^*_y$ is the lateral acceleration estimation coming from the dynamical model considering a constant nominal road friction ($\mu = 1$). $\Delta(\hat{V}_x, \hat{V}_y)$ is a mere scaling factor.

Recall that model (7) assumes steady state cornering. Its accuracy may degrade when the vehicle lateral dynamic is excited. To account for this variable accuracy, k_y switches between two tuning parameters $k_{y_{max}}, k_{y_{min}}$ depending on the kinematic sideslip rate quantity $\dot{\beta}$:

$$k_y = \begin{cases} k_{y_{min}}, & \dot{\beta} \geq \bar{\dot{\beta}} \\ k_{y_{max}}, & \dot{\beta} < \bar{\dot{\beta}}. \end{cases} \tag{12}$$

The parameter takes a higher value ($k_{y_{max}}$) when the tire model is more reliable and a lower one ($k_{y_{min}}$) when the vehicle lateral dynamic is more excited and the integration of the kinematic model state variables derivatives should not suffer drifting issues. The k_y switching condition depends on the kinematic sideslip rate quantity $\dot{\beta}$: the higher $\dot{\beta}$, the more excited the lateral dynamic is. $\dot{\beta}$ can be approximated as:

$$\dot{\beta} = \frac{A_y - \omega_z \hat{V}_x}{\hat{V}_x} \tag{13}$$

and directly calculated from available measures without numerical differentiation. Such scheduled feedback gain approach represents an innovation with respect to [26] which considers a constant k_y. Since k_y takes the best value depending on the lateral dynamic excitation and is no more a constant intermediate value, it fully exploits the hybrid nature of the observer.

2.3 Friction Estimation

The friction estimation algorithm modifies the approach presented in [26] and it consists of two different laws in case of high or low excited vehicle lateral dynamic:

$$\dot{\hat{\mu}} = \begin{cases} K_\mu \cdot (A_y - \hat{A}_y), & \dot{\beta} \geq \bar{\dot{\beta}}_\mu \text{ and } \omega_z \geq \bar{\omega}_z \\ \bar{K}_\mu \cdot (\bar{\mu} - \hat{\mu}), & \dot{\beta} < \bar{\dot{\beta}}_\mu \text{ or } \omega_z < \bar{\omega}_z, \end{cases} \tag{14}$$

where:

$$K_\mu = k_\mu \cdot \hat{A}^*_y \cdot \Delta(\hat{V}_x, \hat{V}_y) \tag{15}$$

In the first case, the innovation term is the same of the lateral dynamic equation. However, the lateral speed $\hat{V}_y$ dynamic is generally faster than the friction coefficient one

and the frequency decoupling can be enforced correctly tuning the feedback gain k_μ. In this way, slow trends of $A_y - \hat{A}_y$ are attributed to friction variation and fast ones to $\hat{V}_y$. The remaining terms $\hat{A}_y^*$ and Δ are the same of the $\dot{\hat{V}}_y$ dynamic equation.

In the second case, the vehicle lateral dynamic is not sufficiently excited (e.g. straight driving, slow turns) and the road surface friction variations do not impact the car behavior, specifically, its lateral acceleration. Therefore, $\hat{\mu}$ slowly tends to a default friction value ($\bar{\mu}$) where $\bar{K_\mu}$ is a tuning parameter defining the attraction speed to $\bar{\mu}$.

The switching law between excited and non excited lateral dynamic conditions is based on $\dot{\beta}$ and the yaw rate ω_z. If both these quantities are greater than specific thresholds ($\bar{\dot{\beta}}_\mu, \bar{\omega}_z$) the lateral dynamic is sufficiently excited.

2.4 Tuning Parameters

To conclude the adaptive observer architecture presentation, the set of tuning parameters $\mathcal{P}$ is here summarized. They are classified in:

1. *dynamical model parameters* $\mathcal{P}_d$: ($a_{C_{F,R}}, b_{C_{F,R}}, a_{k_{F,R}}, b_{k_{F,R}}$) to parametrize the friction dependence;
2. *longitudinal speed estimate $\tilde{V}_x$ parameters* $\mathcal{P}_v$: two (γ_-, γ_+) to implement the longitudinal speed from wheel speed algorithm;
3. *longitudinal dynamic feedback parameters* $\mathcal{P}_x$: feedback gains ($K_{x_{min}}, K_{x_{max}}$) and the switching threshold on the longitudinal acceleration ($\bar{\Delta}_{A_x}$);
4. *lateral dynamic feedback parameters* $\mathcal{P}_y$: feedback gains ($k_{y_{min}}, k_{y_{max}}$) and the switching threshold ($\bar{\dot{\beta}}$);
5. *friction feedback parameters* $\mathcal{P}_\mu$: feedback gains ($k_\mu, \bar{K_\mu}$) and switching thresholds ($\bar{\dot{\beta}}_\mu, \bar{\omega}_z$) .

We tune the observer in two phases. In the first phase, starting from data collected on different road surfaces ($\tilde{\mathcal{D}}$) on an instrumented vehicle, we isolate the steady state maneuvers and identify the tire characteristics in (10) through static curve fitting. The second phase is instead dynamic and consists in finding the remaining parameters that minimize the following cost function:

$$J_\beta(\mathcal{P}) = \left\| \hat{\beta}(t_\beta) - \beta(t_\beta) \right\|_2^2 \tag{16}$$

where t_β are the time instants for which the following conditions apply: (1) Longitudinal velocity is higher than 20 [km/h]). (2) The absolute value of measured sideslip $\beta(t)$ is contained in a fixed region of interest (i.e. $2 < |\beta(t_\beta)| < 12$ [deg]). In this way, we privilege accuracy in the range that is relevant to vehicle dynamics control algorithms [39]. The optimization is run on simulated data, using a numerical gradient descent method. Table 1 summarizes the parameters used in this work.

Parameter	Value	Paramer	Value
a_{C_F}	-44	a_{C_R}	-46
b_{C_F}	57	b_{C_R}	79
γ_-	35 [deg]	γ_+	35 [deg]
$K_{x_{min}}$	0.2	$K_{x_{max}}$	5
$k_{y_{min}}$	0.3	$k_{y_{max}}$	10
k_μ	0.007	$\bar{K_\mu}$	0.08
$\bar{\dot{\beta}}_\mu$	7 [deg]	$\bar{\omega}_z$	5 [deg/s]
$\bar{\dot{\beta}}$	0.3 [deg/s]		

Table 1: Tuning parameters.

3 TYRE/ROAD FRICTION CLASSIFIER

The adaptive state observer module main limitation regards the adaptation to tyre/road friction changes. According to the frequency separation idea, it exploits only slow variations of lateral dynamic innovation term to estimate the friction. Hence, the transient of $\hat{\mu}$ to the new friction value is not always rapid. To improve this, the architecture includes a tire friction classifier. This module promptly detects road condition changes so that the adaptive observer friction estimate is reinitialized to a value closer to the real one and the adaptive observer will just have to refine the estimation. In particular, a classification between high and low friction suffices to significantly reduce the duration of the adaptation phase to friction variations and to improve the sideslip estimation performance. As in Figure (9), the classifier input signals are the vehicle acceleration (A_x, A_y, A_z), the steering angle (δ_f), the wheels speed (V_{w_i}) and the four wheels traction and braking torques (T_{en_i}, T_{br_i}). Note that, given the 4WD electric vehicle application considered, the assumption of known T_{en_i}, T_{br_i} is reasonable. The output signal $\bar{\mu}$ is a boolean which, at every time instant, becomes $\bar{\mu} = 1$ if a low to high friction change is detected and $\bar{\mu} = 0$ when the friction varies from high to low condition. It keeps its last value if no friction variation is detected. Under the assumption of longitudinal and lateral vehicle dynamics decoupling, two independent classifiers run in parallel and

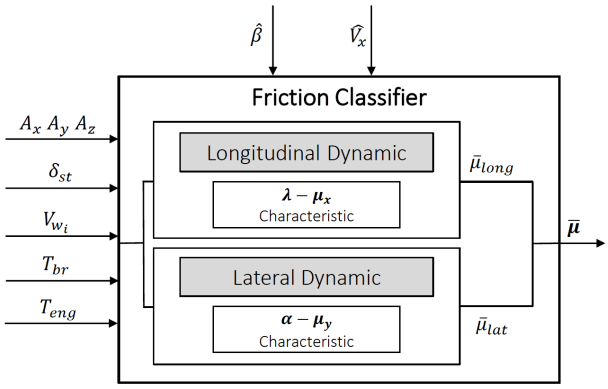

Fig. 9: Friction classifier structure.

follow the same rationale exploiting the road-tire characteristics. The longitudinal dynamic one is based on the

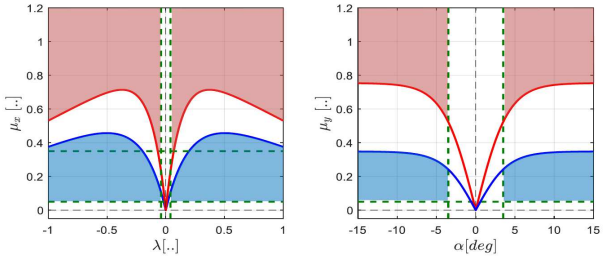

Fig. 10: Longitudinal and lateral friction classification maps.

relation between longitudinal slip λ and the longitudinal instantaneous friction coefficient $\mu_x(t)$. λ is defined as:

$$\lambda_i = \frac{V_{w_i} - \hat{V}_x}{\max(V_{w_i}, \hat{V}_x)} \tag{17}$$

where V_{w_i} and $\hat{V}_x$ are the vehicle longitudinal speed estimate while:

$$\mu_x(t) = \frac{F_x}{F_z}. \tag{18}$$

F_x and F_z are estimates of the longitudinal and vertical forces. For clarity's sake, we now assume these quantities known; postponing the details on their computation to a later paragraph. The left picture of Figure 10 visualizes the classification logic. The map consists of three regions: high grip (red), low grip (blue) and non-defined (white). At each time instant, the algorithm makes a check, if $(\lambda(t), \mu_x(t))$ belongs to the red region and $\bar{\mu} = 0$, a low to high friction classification happens. If $(\lambda(t), \mu_x(t))$ falls in the blue region and $\bar{\mu} = 1$, a high to low friction classification arises. In all other cases, no friction change is identified and $\bar{\mu}$ keeps its last value. In particular, if $(\lambda(t), \mu_x(t))$ is in the white region $\bar{\mu}$ remains always unchanged. The classification procedure is repeated for the four wheels. Note that the method can accomodate for any parametrization of the friction characteristic. In this case, we used a Burkhardt [40] parametrization. The horizontal and vertical dashed green lines are further limits on λ and μ_x. The white area helps to avoid misclassification. Measurement and estimation noises affect both $\lambda(t)$ and $\mu_x(t)$; in case of intermediate $\mu_x(t)$ values or low $\lambda(t)$, this can cause wrong classification. To solve this issue the classifier does not switch when $\lambda(t)$, $\mu_x(t)$ belong to the white region.

The lateral dynamic classifier relies on the relation between wheel slip angle α and the instantaneous lateral friction coefficient $\mu_y(t)$. $\alpha_{F,R}$ are defined by (9) while, exploiting the estimated F_y, F_z:

$$\mu_y(t) = \frac{F_y}{F_z}. \tag{19}$$

The classification logic can be visualized through the right plot of Figure 10 and shares the same reasoning of the longitudinal dynamic classifier. At each time instant, a road friction change is identified depending on the (α, $\mu_y(t)$) location in the corresponding map. The procedure is repeated for the front and rear axles. Worthy to note that the lateral low and high friction (α, $\mu_y(t)$) characteristics consider the same model (8) of the adaptive state observer.

While one can apply (17) and (9) to calculate λ, α using the adaptive observer estimate $\hat{\beta}, \hat{V}_x$, the estimation of the road tire forces F_x, F_y, F_z needed by (18), (19) calls for another estimator.

What follows shows that a relative simple model-based estimation of the forces suffices. $F_z(i)$ comes from the distribution of the full load of the vehicle considering both the car geometry (static load distribution) and the vehicle dynamics effects:

$$F_{z_i} = k_{1_i} mg + k_{2_i} mA_x + k_{3_i} mA_y. \tag{20}$$

where m, g are the vehicle mass and gravity accelerations, A_x, A_y the accelerations at the center of gravity

and $k_{1_i}, k_{2_i}, k_{3_i}$ are constant coefficients depending on car geometry.

$F_x(i)$ is achieved through a single corner model. Assuming to know the braking and traction torques (T_{br}, T_{en}) at the wheel, $F_x(i)$ comes from the following torque balance:

$$F_{x_i} = \frac{T_{en_i} - T_{br_i} - J \cdot \dot{\omega}_i}{R_i}. \tag{21}$$

Finally, F_y results from a steady-state bicycle model whose lateral force balance yields:

$$\begin{aligned} F_y &= m \cdot A_y = F_{y_F} + F_{y_R} \\ F_{y_F} &= \frac{L_r}{L_f + L_r} m A_y \\ F_{y_R} &= \frac{L_f}{L_f + L_r} m A_y. \end{aligned} \tag{22}$$

4 EXPERIMENTAL RESULTS

An experimental campaign on a 4-wheel-drive full electric vehicle thoroughly validates the proposed observer. We performed all experiments on a prototype Sport Utility Vehicle, with a mass of 2590 kg, a wheel base of 2.87 m, a track width of 1.654 m and center of gravity height of around 0.56 m. The observers inputs signals are:

1. accelerations A_x, A_y and yaw rate ω_z from a three degrees of freedom IMU,
2. wheel steering angle δ_f and wheel speeds V_{w_i} from encoders,
3. braking and traction torques T_{br}, T_{en} for the four wheels. Note that the vehicle is equipped with four independent electric motors and thus T_{br}, T_{en} are known.

A set of additional sensors provides reference signals to evaluate the estimation:

1. an optical sensor directly measures the sideslip β and longitudinal speed V_x,
2. a high precision GPS gets the vehicle position on the track. Since the track consists of both high and low grip areas, a precise knowledge of the vehicle location provides the actual road friction at every time instant.

The analysis consists of two parts: the first one examines the adaptive state observer performance on high and low grip conditions; the second one focuses on the improvements achieved thanks to the friction classifier in case of road conditions variations. In particular, the validation analysis investigates abrupt friction variations tests (i.e. μ jump) where the vehicle consecutively crosses low and high friction surfaces while performing aggressive maneuvers. Such validation assesses the relevance of the algorithm innovations in terms of rapid friction changes detection and sideslip estimation and, to the best of the authors knowledge, is extremely rare in the scientific literature.

4.1 Adaptive Observer Validation

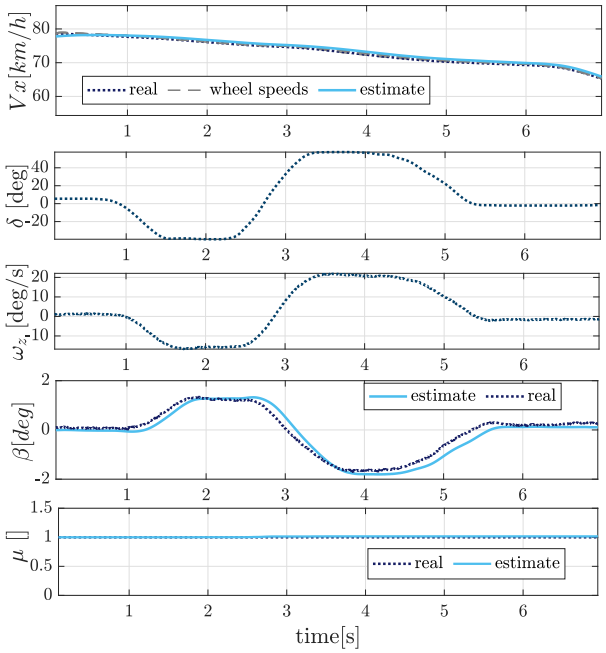

Fig. 11: Longitudinal speed V_x, sideslip angle β and friction μ estimation results on dry asphalt road, estimated at 1 using offline methods.

Figure 11 presents a double lane change maneuver on dry asphalt. The adaptive observer friction is initialized at its actual value $\hat{\mu} = 1$. The three estimates $\hat{V}_x, \hat{\beta}, \hat{\mu}$ from the observer (light blue) almost coincide with the real V_x, β, μ measures (dotted dark blue). Even if small, the observer accurately estimates the sideslip angle $\hat{\beta}$ while the friction parameter correctly keeps $\hat{\mu} = 1$. Figure 12 reports a small section of a handling test on snow, where the higher longitudinal wheels slip caused by the low grip surface makes the estimation more challenging. Note the

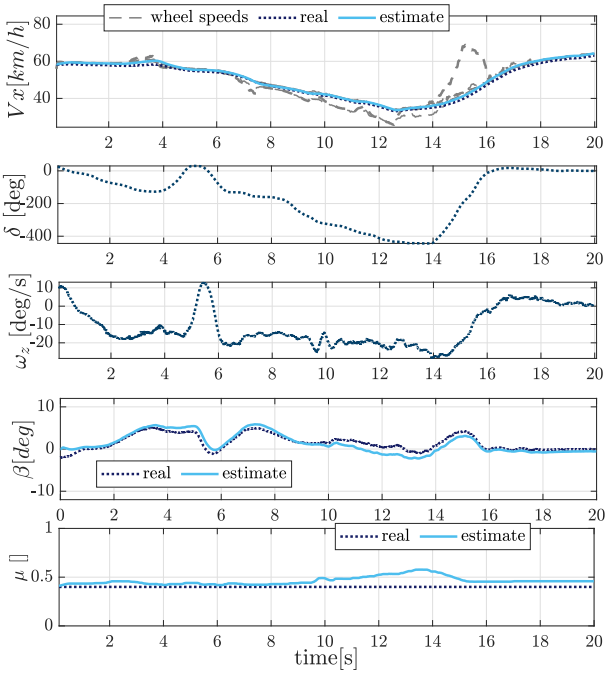

Fig. 12: Longitudinal speed V_x, sideslip angle β and friction μ estimation results on snow, estimated at 0.3 using offline methods.

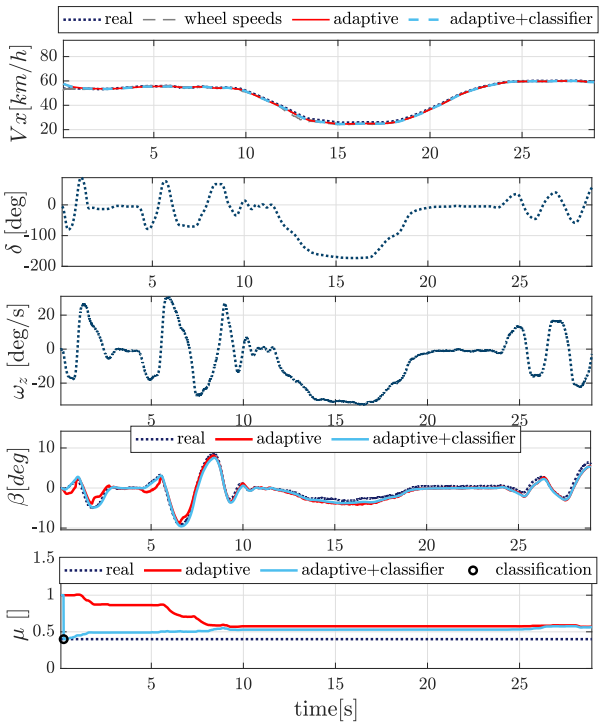

Fig. 13: Adaptation to road friction change: comparison between adaptive state observer module only and full observer architecture.

aggressive change in the steering angle at around 5 seconds, performed to stabilize the vehicle. $\hat{\mu}$ is initialized to the low friction reference $\hat{\mu} = 0.3$. The observer correctly tracks both the sideslip angle and the longitudinal speed even in the $[10, 20]$ s interval when the wheels are slipping. The friction parameter fluctuates around its real value.

4.2 Full Observer Validation: Road Friction Changes Tests

Once the adaptive observer performance is verified for different tyre/road frictions, the following tests address the road conditions variation issue. Figure 13 shows the benefits of the full estimation algorithm including the classifier compared to the pure adaptive state observer. The test contains both aggressive maneuvers and quasi-static ones. The plots compare V_x, β, μ estimates from the full algorithm (light blue) and the one from the pure adaptive observer (red) to the real measures (dotted dark blue) in addition to the steering angle and yaw rate. Both observers are initialized on dry asphalt, $\hat{\mu} = 1$ but at the beginning of the test a road change from dry to wet asphalt happens. One can see that:

1. The full algorithm $\hat{\mu}$ (light blue) immediately jumps to the low grip reference thanks to the prompt classification and then settles to the actual road value.
2. The adaptive state observer without $\hat{\mu}$ re-initialization (red) gradually moves from $\hat{\mu} = 1$ to the final value.
3. The adaptation phase lasts in both cases around 10 s. However, thanks to the classifier, $\hat{\mu}$ is immediately closer to the actual friction and the sideslip estimation accuracy during the transient clearly improves. At 5 s the adaptive observer without classifier (red) $\hat{\beta}$ reaches its maximum estimation error of approximately $\hat{\beta}_{err} = 4.5$ deg while the full observer (light blue) is always reliable and its maximum error is much lower, $\hat{\beta}_{err} = 0.5$ deg at 8.5 s. Note that during this adaptation phase, both observers adapt the friction estimation. The adaptive observer lowers the estimation, while the version with the classifier increases it. As a matter of fact, the low friction initialization underestimates the actual friction. The re-initialization modifies the estimated value more than the proposed approach, as the innovation (the difference between the predicted lateral acceleration and the measured one) is larger.

	μ: low $\rightarrow$ high	μ: high $\rightarrow$ low μ
$\hat{\mu}$: low $\rightarrow$ high	94%	2%
$\hat{\mu}$: high $\rightarrow$ low	2%	80%
no detection	4%	18%

Table 2: Friction change confusion matrix.

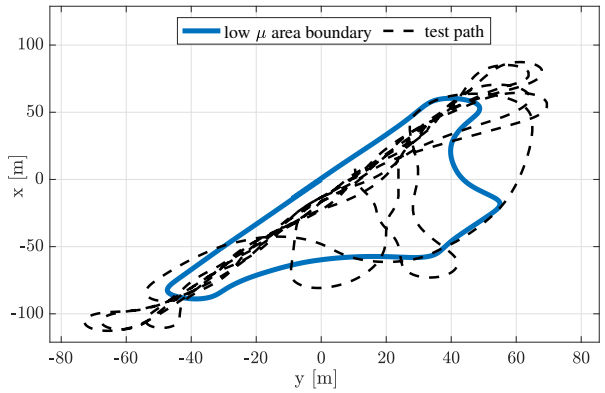

Fig. 14: Consecutive friction changes test: high-low friction areas boundary and vehicle trajectory.

The last experiment specifically validates the friction classifier. The proving ground consists of a low grip area ($\mu = 0.4$) surrounded by a high grip one ($\mu = 1$). The driver consecutively crosses the boundary between the two regions to change the road tire friction conditions. Figure 14 shows the map of the testing area with the low friction area boundaries (blue) and the vehicle path (dashed black). During the 10 min test, the vehicle experienced around 60 friction changes. The classifier correctly recognizes 52 out of 60 changes (87%). Table 2 summarizes the statistics breakdown. The statistics consider a friction change as detected if the state of the observer switches to the correct state before the vehicle leaves that area. The algorithm wrongly classifies a change of friction only in 2% of the instances. Note that the no detection statistics account for all cases in which the vehicle leaves the area before an adequate level of excitation is reached, which does not pose any problem from the side slip angle estimation perspective as the side slip angle is small in those cases.

Figure 15 plots a section of this test and compares the $\hat{V}_x, \hat{\beta}, \hat{\mu}$ estimation of full algorithm (light blue) and pure adaptive observer (red) to the measured references (dotted dark blue) it appears that:

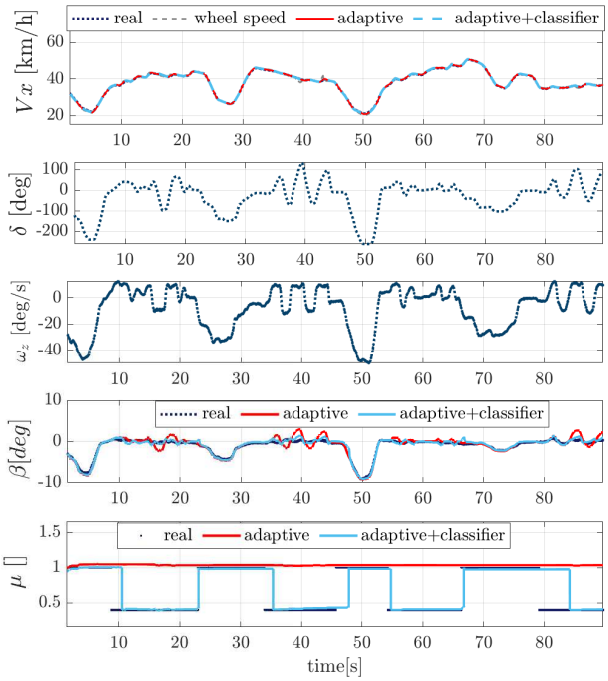

Fig. 15: Consecutive friction changes test: estimation results.

1. only exploiting the classifier, $\hat{\mu}$ correctly tracks the reference. The $\hat{\mu}$ from the pure adaptive observer (red) is not responsive enough to friction changes and almost keeps the value corresponding to dry asphalt. The full observer $\hat{\mu}$ estimate (light blue) switches and tracks the friction variations.
2. The sideslip $\hat{\beta}$ from the full observer (light blue) are close to the reference during both high and low friction intervals.
3. The pure adaptive observer estimate (red) is accurate only on dry road when $\hat{\mu}$ is correctly estimated and presents estimation errors up to 3 deg on wet terrain.

As a further confirmation of the full observer structure advantages, Figure 16 reports the cumulative error plot (i.e. the probability to be below a certain $\hat{\beta}$ estimation error) along with the 99% quantiles. The cumulative error achieved by an adaptive observer run under the assumption of a perfect knowledge of the road friction (dotted dark blue) is the benchmark to evaluate the full (light blue) and pure adaptive observer (red) architectures. It results that:

1. the performance of the full algorithm (light blue) almost corresponds to the reference one (dotted dark blue). The $\hat{\beta}$ estimation error is lower than 1.5 deg

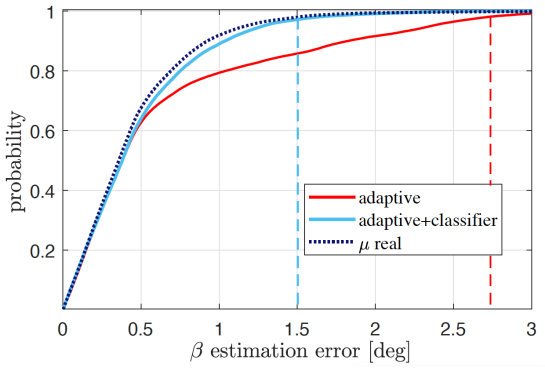

Fig. 16: Consecutive friction changes test: sideslip estimation cumulative error plot.

99% of the times (dashed light blue vertical line).

2. the pure adaptive observer (red) is less accurate and its 99% $\hat{\beta}$ estimation error quantile is around 2.7 deg (dashed red vertical line), 1.2 deg greater than the full observer one.

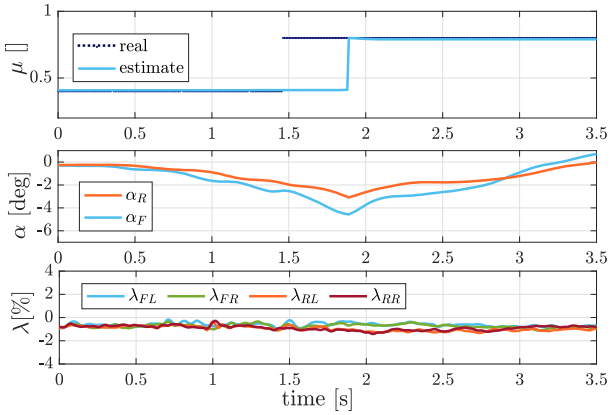

Fig. 17: Consecutive friction changes test: rapid friction change detection $T_c = 0.4$ s.

This type of validation, which is not common in scientific literature due to the complexity of the required experimental set up, offers the chance to investigate the average time needed to recognize the changes in road friction. The average classification time results to be $\bar{T}_c = 2.1$ s with a standard deviation of $\delta_{T_c} = 1.6$ s. The large standard deviation with respect to the average time is due to the fact that the classifier detects friction changes only when either the vehicle longitudinal or the lateral dynamics are sufficiently excited. Therefore, T_c varies depending on the vehicle behavior after the friction change. Figures 17 and 18 exemplify two opposite situations after a low to high friction change. The upper sub-plot of both figures show the real (dark blue) and estimated (light blue) μ estimate; the intermediate and bottom sub-plots show the four wheels estimated longitudinal slip λ and the front and rear slip angles $\alpha_{F,R}$ which provide information about how the maneuvers excite longitudinal and lateral dynamics.

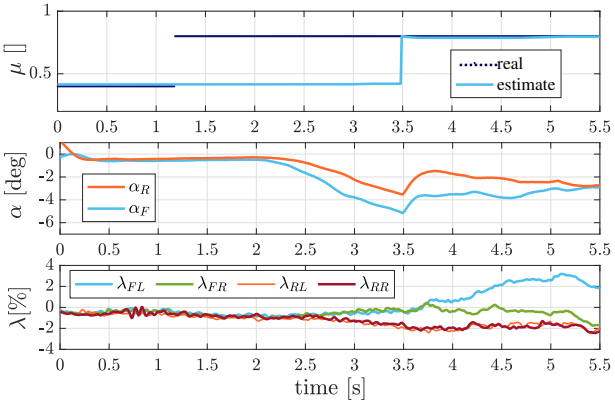

Fig. 18: Consecutive friction changes test: late friction change detection $T_c = 2.3$ s.

Figure 17 refers to a test where an aggressive maneuver (i.e. high λ, α) follows the road friction change at 1.45 s. The classifier immediately reacts and the $\hat{\mu}$ (light blue) jumps to the real value (dark blue) with $T_c = 0.4$ s. In Figure 18 a friction change occurs at 1.45 s but neither λ_i or $\alpha_{F,R}$ start to increase before 2.2 s. Hence, the classification happens only at 3.5 s with $T_c = 2.3$ s. Note that there is no need of rapid μ estimation when vehicle dynamics are not particularly excited since vehicle control systems exploit friction information only when aggressive maneuvers (e.g. emergency maneuvers) must be performed.

In Figure 19, the data from the described μ jump test fill the classifier switching map of Figure 10. The estimated $\lambda - \mu_x$ and $\alpha - \mu_y$ are orange when the vehicle is on high grip and light blue if on low grip. Figure 19 illustrates how estimating μ becomes difficult in low λ, α conditions. $\lambda - \mu_x$ and $\alpha - \mu_y$ boundaries of the two road surfaces (red, blue) are extremely close to one another. Hence, measurement noises and small estimation inaccuracies make the classification almost impossible. In this experiment, a clear differentiation between low and high grip data (orange and light blue) is visible only for $\alpha > 3$

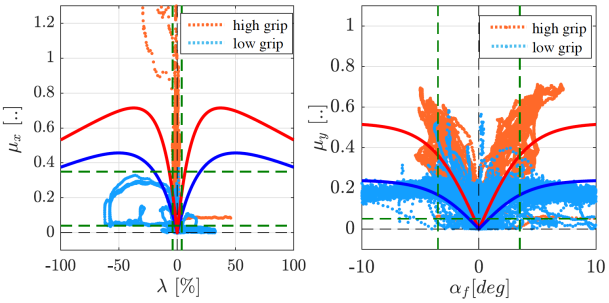

Fig. 19: Consecutive friction changes test: experimental data friction classifier maps.

deg and $\lambda > 0.05$.

5 CONCLUSIONS

This paper proposes a sideslip and friction estimation approach that combines a friction classifier based on road tire longitudinal and lateral characteristics to a sideslip state observer. The former rapidly detects road friction changes monitoring both longitudinal and lateral vehicle dynamics. The latter, based on both vehicle kinematic and dynamic models, provides accurate longitudinal speed, sideslip and refines the friction estimation.

The main goal of the algorithm is to improve sideslip and friction estimation during the adaptation phase following sudden road surface variations. As proved by an extensive experimental validation on a 4WD electric vehicle on different road surfaces, the settling time and the sideslip estimation error are significantly lowered.

REFERENCES

[1] Liebemann, E., Meder, K., Schuh, J., and Nenninger, G., 2004, "Safety and performance enhancement: The bosch electronic stability control (esp)," *SAE Technical Paper*.

[2] Lucchini, A., Formentin, S., Corno, M., Piga, D., and Savaresi, S., 2020, "Torque vectoring for high-performance electric vehicles: an efficient mpc calibration," *IEEE Control Systems Letters,* **4**, pp. 725–730.

[3] Funke, J., Brown, M., Erlien, S., and Gerdes, J., 2017, "Collision avoidance and stabilization for autonomous vehicles in emergency scenarios," *IEEE transactions on control systems technology,* **25**(4), pp. 1204–1216.

[4] Zhang, F., Gonzales, J., Shengbo, E., Borrelli, F., and Li, K., 2018, "Drift control for cornering maneuver of autonomous vehicles," *Mechatronics,* **54**, pp. 167–174.

[5] Hu, C., Wang, R., Yan, F., and Chen, N., 2015, "Should the desired heading in path following of autonomous vehicles be the tangent direction of the desired path?," *IEEE Transactions on Intelligent Transportation Systems,* **16**(6), pp. 3084–3094.

[6] Singh, K. B., Arat, M. A., and Taheri, S., 2019, "Literature review and fundamental approaches for vehicle and tire state estimation," *Vehicle System Dynamics,* **57**(11), pp. 1643–1665.

[7] Manning, W., and Crolla, D., 2007, "A review of yaw rate and sideslip controllers for passenger vehicles," *Transactions of the Institute of Measurement and Control,* **29**(2), pp. 117–135.

[8] Chindamo, D., Lenzo, B., and Gadola, M., 2018, "On the vehicle sideslip angle estimation: A literature review of methods, models, and innovations," *Applied Sciences,* **8**, p. 355.

[9] Bonfitto, A., Feraco, S., Tonoli, A., and Amati, N., 2020, "Combined regression and classification artificial neural networks for sideslip angle estimation and road condition identification," *Vehicle system dynamics,* **58**(11), pp. 1766–1787.

[10] Cerone, V., Piga, D., and Regruto, D., 2011, "Set-membership lpv model identification of vehicle lateral dynamics," *Automatica,* **47**(8), pp. 1794–1799.

[11] Bonfitto, A., Feraco, S., Tonoli, A., and Amati, N., 2020, "Combined regression and classification artificial neural networks for sideslip angle estimation and road condition identification," *Vehicle System Dynamics,* **58**(11), pp. 1766–1787.

[12] Bertipaglia, A., Shyrokau, B., Alirezaei, M., and Happee, R., 2022, "A two-stage bayesian optimisation for automatic tuning of an unscented kalman filter for vehicle sideslip angle estimation," In 2022 IEEE Intelligent Vehicles Symposium (IV), IEEE, pp. 670–677.

[13] Chaichaowarat, R., and Wannasuphoprasit, W., 2016, "Kinematic-based analytical solution for wheel slip angle estimation of a rwd vehicle with drift," *Engineering Journal,* **20**(2), pp. 90–107.

[14] Farrelly, J., and Wellstead, P., 1996, "Estimation of vehicle lateral velocity," *Proceedings of the 1996 IEEE International Conference on Control Applications*, pp. 552–557.

[15] Selmanaj, D., Corno, M., Panzani, G., and Savaresi, S., 2017, "Vehicle sideslip estimation: A kinematic based approach," *Control Engineering Practice,* **67**, pp. 1–12.

[16] Yoon, J.-H., and Peng, H., 2013, "A cost-effective sideslip estimation method using velocity measure-

ments from two gps receivers," *IEEE Transactions on Vehicular Technology,* **63**(6), pp. 2589–2599.

[17] Naets, F., van Aalst, S., Boulkroune, B., El Ghouti, N., and Desmet, W., 2017, "Design and experimental validation of a stable two-stage estimator for automotive sideslip angle and tire parameters," *IEEE Transactions on Vehicular Technology,* **66**(11), pp. 9727–9742.

[18] Cheng, S., Li, L., Yan, B., Liu, C., Wang, X., and Fang, J., 2019, "Simultaneous estimation of tire side-slip angle and lateral tire force for vehicle lateral stability control," *Mechanical Systems and Signal Processing,* **132**, pp. 168–182.

[19] van Hoek, R., Alirezaei, M., Schmeitz, A., and Nijmeijer, H., 2017, "Vehicle state estimation using a state dependent riccati equation," *IFAC-PapersOnLine,* **50**(1), pp. 3388–3393.

[20] Reina, G., Leanza, A., and Mantriota, G., 2022, "Model-based observers for vehicle dynamics and tyre force prediction," *Vehicle System Dynamics,* **60**(8), pp. 2845–2870.

[21] Park, G., 2022, "Vehicle sideslip angle estimation based on interacting multiple model kalman filter using low-cost sensor fusion," *IEEE Transactions on Vehicular Technology*.

[22] Ge, L., Zhao, Y., Zhong, S., Shan, Z., Ma, F., Guo, K., and Han, Z., 2022, "Motion control of autonomous vehicles based on offset free model predictive control methods," *Journal of Dynamic Systems, Measurement, and Control,* **144**(11), p. 111003.

[23] Pacejka, H., ed., 2005, *Tyre and Vehicle Dynamics* Elsevier.

[24] Du, Y., Liu, C., Song, Y., Li, Y., and Shen, Y., 2019, "Rapid estimation of road friction for anti-skid autonomous driving," *IEEE transactions on intelligent transportation systems,* **21**(6), pp. 2461–2470.

[25] Imsland, L., Johansen, T., Fossen, T., Grip, F., Kalkkuhl, J., and Suissa, A., 2006, "Vehicle velocity estimation using nonlinear observers," *Automatica,* **42**, pp. 2091–2103.

[26] Liao, Y.-W., and Borrelli, F., 2019, "An adaptive approach to real-time estimation of vehicle sideslip, road bank angles, and sensor bias," *IEEE Transactions on Vehicular Technology,* **68**(8), pp. 7443–7454.

[27] Grip, H., Imsland, L., Johansen, T., and Fossen, T., 2007, "Nonlinear vehicle side-slip estimation with friction adaptation," *IFAC: Automatica*.

[28] Li, L., Jia, G., Ran, X., Song, J., and Wu, K., 2014, "A variable structure extended kalman filter for vehicle sideslip angle estimation on a low friction road," *Vehicle System Dynamics,* **52**(2), pp. 280–308.

[29] Baffet, G., Charara, A., and Lechner, D., 2009, "Estimation of vehicle sideslip, tire force and wheel cornering stiffness," *Control Engineering Practice,* **17**(11), pp. 1255–1264.

[30] Best, M., Gordon, T., and Dixon, P., 2000, "An extended adaptive kalman filter for real-time state estimation of vehicle handling dynamics," *Vehicle System Dynamics,* **34**(1), pp. 57–75.

[31] Piyabongkarn, D., Rajamani, R., Grogg, J. A., and Lew, J. Y., 2008, "Development and experimental evaluation of a slip angle estimator for vehicle stability control," *IEEE Transactions on control systems technology,* **17**(1), pp. 78–88.

[32] Qin, Y., Wang, Z., Xiang, C., Hashemi, E., Khajepour, A., and Huang, Y., 2019, "Speed independent road classification strategy based on vehicle response: Theory and experimental validation," *Mechanical Systems and Signal Processing,* **117**, pp. 653–666.

[33] Viehweger, M., Vaseur, C., van Aalst, S., Acosta, M., Regolin, E., Alatorre, A., Desmet, W., Naets, F., Ivanov, V., Ferrara, A., et al., 2020, "Vehicle state and tyre force estimation: demonstrations and guidelines," *Vehicle System Dynamics*, pp. 1–28.

[34] Grip, H. F., Imsland, L., Johansen, T. A., Kalkkuhl, J. C., and Suissa, A., 2009, "Vehicle sideslip estimation," *IEEE Control Systems Magazine,* **29**(5), pp. 36–52.

[35] Acosta, M., Kanarachos, S., and Blundell, M., 2017, "Road friction virtual sensing: A review of estimation techniques with emphasis on low excitation approaches," *Applied Sciences,* **7**, p. 1230.

[36] Gustafsson, F., 1998, "Monitoring tire-road friction using the wheel slip," *IEEE Control Systems Magazine,* **18**, pp. 42–49.

[37] Selmanaj, D., Corno, M., and Savaresi, S. M., 2019, "Friction state classification based on vehicle inertial measurements," *IFAC-PapersOnLine,* **52**(5), pp. 72–77.

[38] Muller, S., Uchanski, M., and Hedrick, K., 2003, "Estimation of the maximum tire-road friction coefficient," *J. Dyn. Sys., Meas., Control,* **125**(4), pp. 607–617.

[39] Galluppi, O., Corno, M., and Savaresi, S. M., 2018, "Mixed-kinematic body sideslip angle estimator for high performance cars," In 2018 European Control Conference (ECC), IEEE, pp. 941–946.

[40] Vignati, M., and Sabbioni, E., 2022, "A cooperative control strategy for yaw rate and sideslip angle control combining torque vectoring with rear

wheel steering," *Vehicle System Dynamics,* **60**(5), pp. 1668–1701.

[41] Burckhardt, M., 1993, "Fahrwerktechnik: Radschlupf-regelsysteme, 1993," *Vogel-Verlag, Würtzburg,* **36**.